



1 **A Correction Algorithm for Rotor-Induced Airflow and**
2 **Flight Attitude Changes during Three-Dimensional Wind**
3 **Speed Measurements Made from A Rotary Unmanned**
4 **Aerial Vehicle**

5 Yanrong Yang¹⁺, Yuheng Zhang¹⁺, Tianran Han¹, Conghui Xie², Yayong Liu², Yufei
6 Huang¹, Jietao Zhou¹, Haijiong Sun¹, Delong Zhao³, Kui Zhang⁴, Shao-Meng Li^{1*}

7 ¹College of Environmental Sciences and Engineering, Peking University, Beijing 100871, China

8 ²Laboratory of Gas Instrument Testing, Center for Environmental Metrology, National Institute of
9 Metrology, Beijing 100029, China

10 ³Beijing Weather Modification Center, Beijing 100089, China

11 ⁴Beijing Wisdominc Technology Co., Ltd, Beijing 100070, China

12 +Contributed equally to the work

13 *Correspondence to: Shao-Meng Li (shaomeng.li@pku.edu.cn)*

14 **Abstract.** A hexacopter unmanned aerial vehicle (UAV) was fitted with a three-dimensional sonic
15 anemometer to measure three-dimensional wind speed. To obtain accurate results for three-dimensional
16 wind speeds, we developed an algorithm to correct biases caused by the rotor-induced airflow
17 disturbance, UVA movement, and attitude changes in the three-dimensional wind measurements. The
18 wind measurement platform was built based on a custom-designed integration kit that couples
19 seamlessly to the UAV, equipped with a payload and the sonic anemometer. Based on an accurate digital
20 model of the integrated UAV-payload-anemometer platform, computational fluid dynamics (CFD)
21 simulations were performed to quantify the wind speed disturbances caused by the rotation of the UAV's
22 rotor on the anemometer during the UAV's steady flight under headwind, tailwind, and crosswind
23 conditions. Through analysis of the simulated data, regression equations were developed to predict the
24 wind speed disturbance, and the correction algorithm for rotor disturbances, motions, and attitude
25 changes was developed. To validate the correction algorithm, we conducted a comparison study in which
26 the integrated UAV flew around a meteorological tower on which three-dimensional wind measurements
27 were made at multiple altitudes. The comparison between the corrected UAV wind data and those from
28 the meteorological tower demonstrated an excellent agreement. The corrections result in significant
29 reductions in wind speed bias caused mostly by the rotors, along with notable changes in the dominant
30 wind direction and wind speed in the original data. The algorithm enables reliable and accurate wind

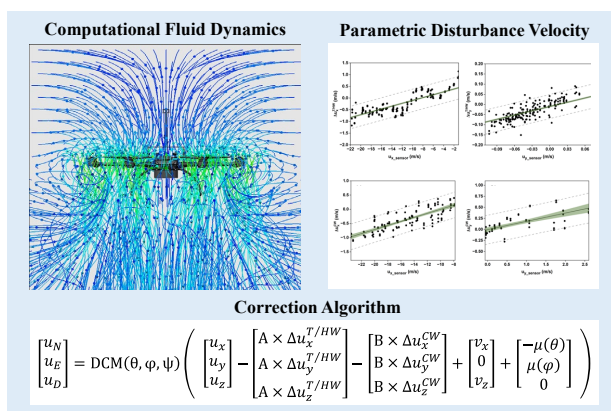


31 speed measurements in the atmospheric boundary layer made from rotorcraft UAVs.

32 **Keywords:** UAV; Rotor Disturbance; Three-dimensional Wind; Correction Algorithm

33

34 **Graphical abstract:**



35

36 **1 Introduction**

37 Wind measurement is crucial in various fields of research and application, including meteorology
 38 and environmental sciences. Accurate wind characteristics facilitate modeling of atmospheric transport
 39 patterns (Gryning et al., 1987; Stockie, 2011), remote sensing data verification (Drob et al., 2015), model
 40 input data assimilation (Gousseau et al., 2011; Vardoulakis et al., 2003) and digital modeling result
 41 optimization (Booij et al., 1999; Van Hooff and Blocken, 2010). In particular, wind profile measurements
 42 near surface can improve the understanding of atmospheric boundary layer (ABL) dynamics and
 43 micrometeorological turbulence at the surface (Seibert et al., 2000), allowing detailed understandings
 44 and model description of energy and mass exchanges between air and surfaces and transport processes.

45 The recent development of unmanned aerial vehicles (UAVs) has provided an opportunity for the
 46 measurement of wind fields in three dimensions with high spatial resolutions (Mcgonigle et al., 2008;
 47 Martin et al., 2011; Kim and Kwon, 2019). The small size, low flight altitude, high mobility and ability
 48 to assemble sensing devices make UAVs ideal platforms from which to measure wind in the ABL
 49 (Thielicke et al., 2021; Shaw et al., 2021; Stewart et al., 2021). Multirotor UAVs allow flexible control
 50 of flight attitude and stationary hovering, and can carry varying payloads depending on the number of
 51 rotors (Villa et al., 2016; Riddell, 2014; Bonin et al., 2013; Stewart et al., 2021), offering significant



52 advantages in capturing high-resolution wind characteristics in low-altitude conditions (Anderson and
53 Gaston, 2013; Mcgonigle et al., 2008).

54 UAVs are often employed to measure wind characteristics both directly and indirectly. Indirect
55 measurement methods involve utilizing pre-installed sensors on the UAV (Elston et al., 2015), in
56 conjunction with specialized flight patterns and wind retrieval algorithm (Bonin et al., 2013; Rautenberg
57 et al., 2018; Gonzalez-Rocha et al., 2019) to achieve wind speed measurement. Although this method is
58 straightforward to operate, it does not accurately reflect actual wind conditions during flight. Direct
59 measurement methods entail installing additional wind sensors on the UAV to obtain real-time wind
60 information in the field. Porous probes (Soddell et al., 2004; Spiess et al., 2007), pitot tubes (Niedzielski
61 et al., 2017; Langelaan et al., 2011), and anemometers (Rogers and Finn, 2013; Nolan et al., 2018) are
62 commonly used sensors. Sonic anemometers are a more prevalent choice for rotorcraft UAVs, capable
63 of measuring wind speed by detecting changes in the speed of sound travel between different sensors
64 (Thielicke et al., 2021). Due to the increasing use of rotorcraft UAVs for wind measurements, sonic
65 anemometers are recognized as one of the most promising methods in terms of measurement accuracy
66 and precision.

67 Sonic anemometers have been mounted onto rotary-wing UAVs for measuring wind speed to
68 varying degrees of success. Typically, an anemometer is mounted at a position along the central axis
69 above the UAV, with data adjusted for the additional wind speed signals induced by UAV motion and
70 attitude changes. Nevertheless, the strong airflow perturbations caused by the rotating propellers can
71 distort real wind flow patterns and significantly affect the accuracy of wind measurements (De Divitiis,
72 2003). However, these distortions were not considered in the adjustment algorithms. To address this
73 issue, researchers have developed several new correction methods. The first method involves mounting
74 the anemometer along the central axis high above the UAV where the rotor wash effects are believed to
75 be limited on the wind speed measurement (Shimura et al., 2018; Barbieri et al., 2019). However, it may
76 not be suitable for hexacopters and octocopters due to the high position required, which may raise safety
77 and flight control concerns. The second method involves new corrections based on experiments in an
78 indoor area to measure wind velocity signal bias caused by the rotors during flight and then subtracting
79 the bias (Palomaki et al., 2017). However, this method is limited by the size of the indoor area,
80 inadequate for full simulations of real UAV rotor speed and attitude changes during flight, and



81 insufficient for the development of a comprehensive correction scheme. Additionally, it does not take
82 into account the detailed coupling of true winds with propeller downwash. The third method is similar
83 to the second except the use of wind tunnels to establish a more accurate relationship between increased
84 air speed and UAV motion or attitude parameters (Thielicke et al., 2021; Neumann and Bartholmai,
85 2015). While effective in determining numerical relationships, the method is limited by the high cost of
86 wind tunnel experiments, and more importantly, by the additional errors introduced by reflected airflows
87 from the wind tunnel walls and ground, as well as the same issues of full simulations of real UAV rotor
88 speed and attitude changes during flight.

89 The flaws in these correction methods could be addressed by using computational fluid dynamics
90 (CFD) simulations to analyze the airflow generated by the UAV's propellers. As far as we know, CFD
91 has been employed to analyze airflow patterns around drones but hasn't been utilized to correct wind
92 measurements obtained from UAVs (Oktay and Eraslan, 2020; Hedworth et al., 2022). In this paper, we
93 introduce a three-dimensional wind speed correction algorithm for sonic anemometer wind
94 measurements taken from a rotary UAV. This algorithm considers the rotor-induced airflow of the UAV,
95 based on CFD simulations, along with the UAV's motion and attitude changes during flight. The
96 accuracy of the algorithm is confirmed by comparing the corrected wind speeds with those measured
97 from a meteorological tower at multiple altitudes. These results could contribute to ongoing efforts
98 aimed at enhancing the performance and reliability of UAV-based wind speed measurement techniques.
99 Additionally, they pave the way for potential applications, such as quantifying pollutant emissions from
100 industrial complexes (Han T, 2023).

101 **2 Method**

102 **2.1 Equipment and Digital Model Representation**

103 A six-rotor UAV (KWT-X6L-15, ALLTECH, China), equipped with six 32 cm diameter propellers
104 driven by M10 KV100 brushless DC motors, was the platform from which wind was measured. The
105 UAV has a symmetrical motor wheelbase of 1765 mm with an unloaded takeoff weight of 22.5 kg and
106 a maximum flight speed of 18 m s⁻¹. It has a flight endurance > 30 min while carrying its maximum
107 payload of 15 kg.

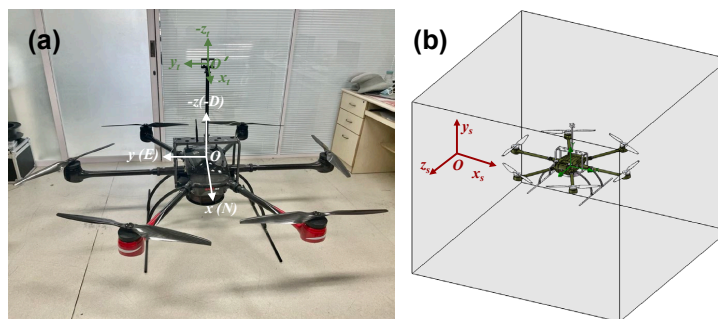
108 A miniature three-dimensional ultrasonic anemometer (Trisonica-Mini Wind and Weather Sensor,



109 Anemoment, America) allowed the measurement of wind speed under 15 m s^{-1} with an accuracy of \pm
110 0.1 m s^{-1} and a resolution of 0.1 m s^{-1} , and wind direction of $0 - 360^\circ$ with an accuracy of $\pm 0.1^\circ$ and a
111 resolution of 0.1° . It was set at 70 cm above the plane of the propellers of the UAV, mounted on a custom-
112 design carbon fiber tube and frame which was further mounted onto a rectangular carbon fiber support
113 base attached to the underbelly of the UAV body, to minimize the effect of propellers-induced flow on
114 the anemometer measurement. The x_r - y_r - z_r coordinate axes of the anemometer, with its center as the
115 origin, were set to be parallel to the x - y - z axes of the aircraft body frame. The mounting of the three-
116 dimensional anemometer is shown in Fig. 1(a).

117 A base digital model of the UAV was provided by its manufacturer for the present CFD simulations.
118 The digital model was further augmented with the accurate digital representation of the three-
119 dimensional anemometer and its mounting frame. Furthermore, considering that the UAV wind
120 measurements are usually tied to other air measurement applications, necessitating additional payload
121 attached to the UAV underbelly simultaneously. Such a payload on the UAV needs also to be included
122 in the digital model for the CFD simulation. In the present case, we added the digital model of a 6.37 kg
123 air sampler developed in our group (Yang et al., 2024) to the UAV base digital model (Fig. 1(b)).

124 For CFD simulations, the complete digital model for the UAV and its payloads was set in the x_s - y_s -
125 z_s simulation coordinate system in Solidworks, a computational fluid simulation tool, on a one-to-one
126 scale (Fig. 1(b)).



127
128 **Figure 1: The establishment of the coordinate system and numerical simulation model for the UAV wind**
129 **measurement platform. (a) The UAV wind speed measurement platform. (b) The digital model of the UAV**
130 **wind measurement platform in the 3D CFD model simulation domain.**

131 2.2 Simulation Scenarios

132 For the UAV flight simulation, we considered over a hundred flight envelope scenarios, including



133 parameters such as UAV flight altitude, wind direction, and wind speed. Since the UAV's predominant
 134 flights are within the atmospheric boundary layer, characterized by significant variability in wind speed
 135 and directions, a flight envelope for the UAV in the simulated environments was setup for the complete
 136 UAV digital model for flight altitudes of 30 and 1000 meters, respectively. These flight envelopes were
 137 designed for the UAV to subject to headwind, tailwind, and crosswind relative to its flight direction.
 138 Under the constraint that the UAV can only operate under true wind speeds $\leq 18 \text{ m s}^{-1}$, and assuming the
 139 applicability of the correction algorithm to most flight scenarios, CFD simulations were conducted for
 140 the UAV under these three wind directions. The simulations encompassed the following flight envelopes
 141 as listed in Table 1: the UAV flew at ground speeds of 18, 14, 10, and 8 m s^{-1} , respectively, and adapted
 142 to wind speeds of 1.5, 3.3, 5.4, 7.9, 10.7, and 14 m s^{-1} .

143 **Table 1: The simulation flight envelope scenarios for the UAV-based wind measurement platform.**

Wind Type	Ground Speed (m s ⁻¹)	Wind speed (m s ⁻¹)	Wind Type	Ground Speed (m s ⁻¹)	Wind speed (m s ⁻¹)	Wind Type	Ground Speed (m s ⁻¹)	Wind speed (m s ⁻¹)
		1.5			1.5			1.5
		3.3			3.3			3.3
	8	5.4		8	5.4		8	5.4
		7.9			7.9			7.9
		10.7			10.7			10.7
								14
		1.5			1.5			1.5
		3.3			3.3			3.3
	10	5.4		10	5.4		10	5.4
		7.9			7.9			7.9
		10.7			10.7			10.7
								14
Tailwind		1.5	Headwind		1.5	Crosswind		1.5
		3.3			3.3			3.3
	14	5.4		14	5.4		14	5.4
		7.9			7.9			7.9
		10.7			10.7			10.7
								14
		1.5			1.5			1.5
		3.3			3.3			3.3
	18	5.4		18	5.4		18	5.4
		7.9			7.9			7.9
		10.7			10.7			10.7
								14



144 2.3 Flight Parameters

145 The movements of the UAV through air, including takeoff, ascent/descent, attitude changes, turning,
146 and horizontal flights, are driven by the rotary propellers, whose power requirement is closely tied to the
147 weights of the UAV and its payload as well as the relative motions of the UAV in air. During a normal
148 flight, the UAV adjusts its inclination angle and propeller speeds in order to achieve a set ground speed
149 for flight. By analyzing the gravity G , pull T and wind resistance D experienced by the UAV under flight
150 conditions, its inclination angle θ and propeller rotation speed M can be calculated according to Eqs. (1)
151 - (5) (Quan, 2017).

$$152 \tan\theta \times mg = D, \quad (1)$$

$$153 p \times (\sin\theta \times S_{xoy} + \cos\theta \times S_{xoz}) = D, \quad (2)$$

$$154 0.5\rho(V_{wind} + V_{UAV})^2 = p, \quad (3)$$

$$155 \cos\theta \times mg = T, \quad (4)$$

$$156 T = C_T \times \rho \times \left(\frac{M}{60}\right)^2 \times D_p^4, \quad (5)$$

157 where θ is the inclination angle of the UAV; m is the combined weight of the UAV and the payloads (i.e.,
158 the air sampler and the anemometer along with its installation frame in the present case), calculated to
159 be 28.869 kg; g is the gravitational constant at 9.8 m s⁻²; D is the wind resistance in Newtons; V_{wind} is
160 the wind speed in m s⁻¹; V_{UAV} is the ground speed of the UAV in m s⁻¹; p is the wind pressure on the UAV
161 in N/m²; S_{xoy} and S_{xoz} are the projected surfaces of the UAV in the horizontal direction and vertical
162 directions, determined to be 0.296 and 0.229 m², respectively; C_T is the rotor pull coefficient with an
163 experimentally determined value of 0.048542; D_p is the UAV propeller diameter at 0.8128 m; ρ is the
164 air density in kg m⁻³; T is each rotor pull in Newton; M is the rotation speed of the rotors in RPM.

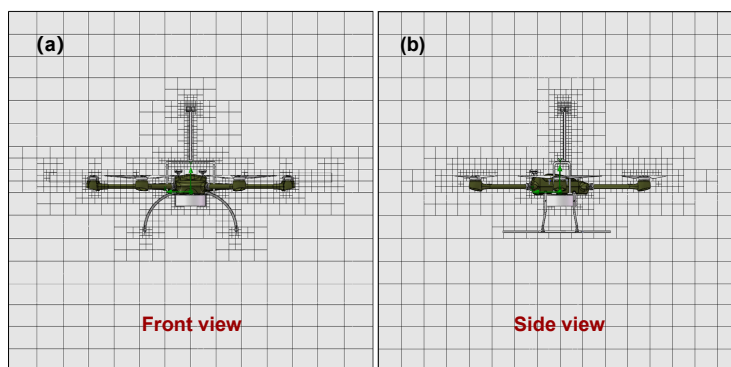
165 Each set of flight condition parameters that constitute the full flight envelope, including wind
166 directions, wind speeds, airspeeds, ground speed, inclination, wind resistance, pull, and M . The CFD
167 simulations were performed to determine the simulated wind fields for each set of parameters in the
168 flight envelope one at a time.

169 2.4 Simulation Parameters

170 The simulation parameters primarily include the computational domain and mesh, fluid and
171 environmental properties, as well as the rotating region. During the CFD flow simulations of the UAV



172 using Solidworks, the computational domain was set to $3.3 \times 3.3 \times 3.3 \text{ m}^3$ according to the wingspan of
173 the UAV, with the complete UAV plus payload digital model set at the center of the domain. The
174 computational domain was divided into two parts with different spatial resolutions based on the grid
175 sizes, considering the computational time and accuracy required for resolving the details of the digital
176 UAV model. The first part was the global domain with a grid size of $0.23 \times 0.23 \times 0.23 \text{ m}^3$, providing a
177 lower spatial resolution. The second part was a nested subdomain within the global domain, specifically
178 defined for the position and dimensions of the anemometer to simulate the measured velocities. The grid
179 size for this nested subdomain was set at $0.0125 \times 0.0125 \times 0.0125 \text{ m}^3$, providing a higher spatial
180 resolution. The total number of grids in the computational domain was 1.11×10^8 , and the specific grid
181 configurations are shown in the Fig. 2. The fluid was modeled as air with characteristics of turbulent
182 and laminar flow, with a turbulence intensity of 0.1% and a turbulence length scale of 0.012 m. The
183 atmospheric pressure was adjusted to 1.01×10^5 and $9.00 \times 10^4 \text{ Pa}$ at altitudes of 30 m and 1000 m,
184 respectively, and the atmospheric temperature was assumed to be $25 \text{ }^\circ\text{C}$ at both altitudes. The relative
185 humidity at different altitudes was determined based on the prescribed pressure and temperature
186 corresponding to each altitude. The UAV's airspeed and aerodynamic angles were configured according
187 to the different flight parameters described in Sect. 2.2 and 2.3. To represent the rotor digitally, six virtual
188 cylinders of the same volume were used to encapsulate the six rotors, with their circumferences match
189 the rotating trajectory of the propeller tip. These virtual cylinders were treated as the rotational regions
190 in the CFD simulation, with their rotation directions aligned with the actual rotation direction of the
191 UAV's propellers. The rotation direction from rotor No. 1 to 6 was alternately clockwise and
192 counterclockwise, and the rotation speed for each flight condition was obtained from Eqs. (1) - (5).



193
194 **Figure 2: Grid configuration of the computational domain.**



195 To ensure relatively accurate simulations, two categories of flow field properties were specified as
196 computational objectives prior to the start of the simulations, and the simulations were terminated upon
197 convergence of the simulation results for all objectives. The first category comprised global domain
198 computational objectives, including average total pressure (P_G), average velocity (V_G), average vertical
199 velocity (V_{Gy}), and average forward velocity (V_{Gz}), where the subscript G denotes the global domain.
200 The second category consisted of subdomain computational objectives, which included the average
201 velocity (V_s), three-dimensional average speed components V_{sx} , V_{sy} , and V_{sz} at the anemometer position
202 in the simulation coordinate system.

203 Upon simulation completion, these velocity components (V_{sx} , V_{sy} , V_{sz}) were further converted to
204 velocity components at the anemometer sensor position (u_{x_sensor} , u_{y_sensor} , u_{z_sensor}) in the airframe
205 coordinate according to Eqs. (6) - (8) below. The converted velocities, u_{x_sensor} , u_{y_sensor} , u_{z_sensor} , were
206 subtracted from the wind velocity (denoted as u_{x_air} , u_{y_air} , and u_{z_air}) setting for each CFD
207 simulation, to estimate the false wind signals arising from the induced flow by the UAV rotors, expressed
208 with Δu_x , Δu_y and Δu_z , respectively, using Eqs. (9) - (11).

209
$$u_{x_sensor} = -V_{sz}, \quad (6)$$

210
$$u_{y_sensor} = V_{sx}, \quad (7)$$

211
$$u_{z_sensor} = -V_{sy}, \quad (8)$$

212
$$\Delta u_x = u_{x_sensor} - u_{x_air}, \quad (9)$$

213
$$\Delta u_y = u_{y_sensor} - u_{y_air}, \quad (10)$$

214
$$\Delta u_z = u_{z_sensor} - u_{z_air}, \quad (11)$$

215 In other words, the false wind signals Δu_x , Δu_y and Δu_z are the terms that must be determined and
216 corrected for in the wind measurements from the UAV.

217 **3 Result and Discussion**

218 **3.1 Example Analysis of Simulation Results**

219 According to the Sect. 2.2, this study develops a series of simulation scenarios for the UAV digital
220 model under various combinations of altitude (30 and 1000 m), wind direction (tailwind, headwind, and
221 crosswind), ground speed (8 to 18 m/s), and wind speed (1.5 to 14 m/s). Six representative simulation
222 scenarios were selected for analysis as examples. These scenarios include UAV flight simulations at

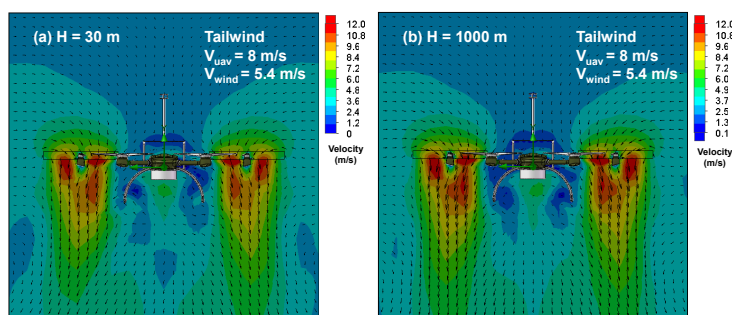


223 altitudes of 30 m and 1000 m, with a ground speed of 8 m/s and a wind speed of 5.4 m/s, under tailwind,
224 headwind, and crosswind conditions. Fig. 3 to 5 present cross-sectional views of the surrounding flow
225 fields during UAV flight under these conditions. In the figures, color gradients represent the magnitude
226 of the velocity, while arrows indicate both the direction and magnitude of the velocity. Overall, under
227 varying wind conditions, the direction and speed of airflow around the UAV show significant differences.
228 While the airflow direction around the UAV remains relatively consistent at the both simulation altitudes,
229 the airflow speed at 1000 m is slightly higher than at 30 m, particularly under tailwind conditions.
230 Specifically, based on the ground speed, wind direction, and wind speed settings, the UAV's airspeed
231 relative to the wind is 2.6 m/s, 13.4 m/s, and 5.4 m/s in tailwind, headwind, and crosswind scenarios,
232 respectively.

233 As show in Fig. 3 (a) and (b), in the tailwind scenario, the maximum downwash velocity occurs
234 directly beneath the UAV rotors, with the airflow directed vertically downward. The next highest
235 velocities are observed around the sides and above the rotors, where the airflow follows an inward and
236 downward trend. The wind speed at the anemometer location is minimally influenced by the UAV rotors,
237 meaning the measured wind speed represents the true airspeed. In the headwind scenario (Fig. 4 (a) and
238 (b)), the highest airflow velocity is detected near the area directly above the rotors, with the airflow also
239 following an inward and downward pattern. The lowest velocity is found directly below the rotors, where
240 the airflow moves upward and outward. At the anemometer's location, some interference from the UAV
241 rotors is present, so the wind speed at this point is a combination of the true airspeed and the rotor-
242 induced velocity. As exhibited in Fig. 5 (a) and (b), in the crosswind scenario with wind blowing from
243 left to right, the airflow around the UAV resembles that in the headwind scenario, but the overall flow
244 field is deflected to the right due to the crosswind, with relatively lower airflow velocity. In the scenario
245 with wind blowing from right to left, the flow field shifts to the left. These results show that the flow
246 field around the UAV varies significantly depending on wind direction, and the anemometer experiences
247 different levels of interference accordingly. Thus, accurately quantifying the interference of the UAV
248 rotors on the anemometer is essential.



249



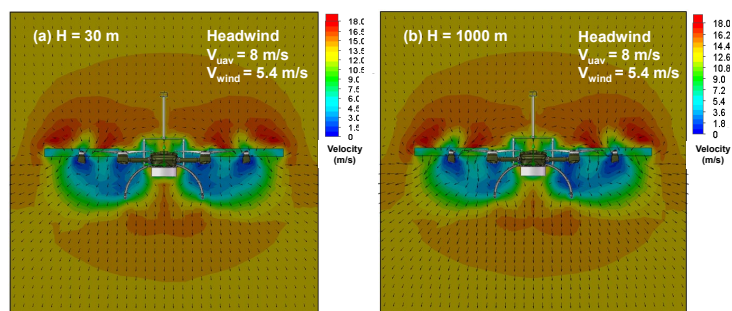
250

Figure 3: Simulation flow field example results of the UAV wind measurement platform in the tailwind scenario. (a) and (b) represent the longitudinal cross-sections of the simulation flow fields for the UAV at altitudes of 30 m and 1000 m, with a ground speed of 8 m/s and a wind speed of 5.4 m/s.

251

252

253



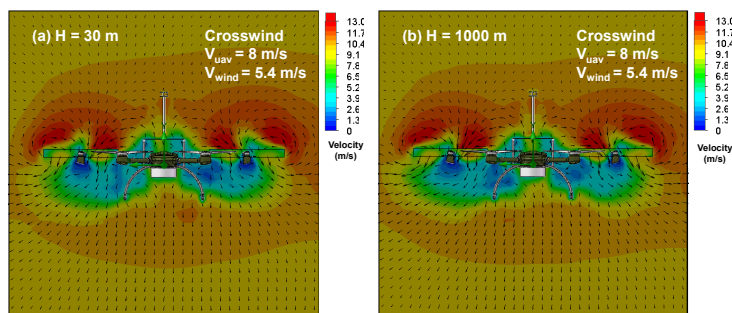
254

Figure 4: Simulation flow field example results of the UAV wind measurement platform in the headwind scenario. (a) and (b) represent the longitudinal cross-sections of the simulation flow fields for the UAV at altitudes of 30 m and 1000 m, with a ground speed of 8 m/s and a wind speed of 5.4 m/s.

255

256

257



258

Figure 5: Simulation flow field example results of the UAV wind measurement platform in the crosswind scenario. (a) and (b) represent the longitudinal cross-sections of the simulation flow fields for the UAV at altitudes of 30 m and 1000 m, with a ground speed of 8 m/s and a wind speed of 5.4 m/s.

259

260

261

3.2 The effect of flight altitude on rotor interference with anemometer measurements

262

Through simulating the flight of UAV in all simulation scenarios, the false signals produced by the



263 UAV rotors on the anemometer at different altitudes and wind characteristics were captured. Initially,
 264 the influence of flight altitude on the false signals was examined.

265 The simulated flight data under tailwind and headwind conditions were integrated into a unified
 266 data set since the UAV flight velocity vector is parallel to the tailwind and headwind velocity vectors
 267 during normal flight. The simulated false wind signals on the anemometer in the airframe x , y , and z
 268 directions, caused by the propeller induced airflow under tailwind and headwind conditions, were
 269 represented by $\Delta u_x^{T/HW}$, $\Delta u_y^{T/HW}$, and $\Delta u_z^{T/HW}$, respectively. For the tailwind and headwind datasets,
 270 according to the Wilcoxon non-parametric test for paired samples, as shown in Table 2, the differences
 271 in $\Delta u_x^{T/HW}$, $\Delta u_y^{T/HW}$ and $\Delta u_z^{T/HW}$ were not significant ($p < 0.05$) at either the 30 m or the 1000 m
 272 altitudes. Therefore, in the presence of tailwind or headwind, the interference from the UAV propeller-
 273 induced flow on the anemometer measurement can be considered independent of the flight altitude in
 274 this altitude range.

275 Similarly, the simulated false wind signals on the anemometer in the x , y , and z directions were
 276 represented by Δu_x^{CW} , Δu_y^{CW} , and Δu_z^{CW} . The Wilcoxon non-parametric test of paired samples was
 277 also applied (shown in Table 1) between the two altitudes. No significant differences were found for
 278 Δu_x^{CW} , Δu_z^{CW} between the two altitudes, but there was an obvious discrepancy for Δu_y^{CW} ($p = 0.00$)
 279 at the two altitudes. This indicates that under cross wind conditions, the disturbances of the UAV
 280 propeller in the x and z directions of the anemometer are not altitude dependent, but that in the y (upward)
 281 direction it is necessary to distinguish the altitude.

282 **Table 2: Wilcoxon nonparametric tests for paired samples of false wind velocity signals between 30 m and**
 283 **1000 m flight altitudes.**

Wind Types	False Wind Signal	Significance	α	Test results
Tailwind/Headwind	$\Delta u_x^{T/HW}$	0.93	0.05	No difference
	$\Delta u_y^{T/HW}$	0.72	0.05	No difference
	$\Delta u_z^{T/HW}$	0.21	0.05	No difference
Crosswind	Δu_x^{CW}	0.36	0.05	No difference
	Δu_y^{CW}	0.00	0.05	Significant difference
	Δu_z^{CW}	0.81	0.05	No difference



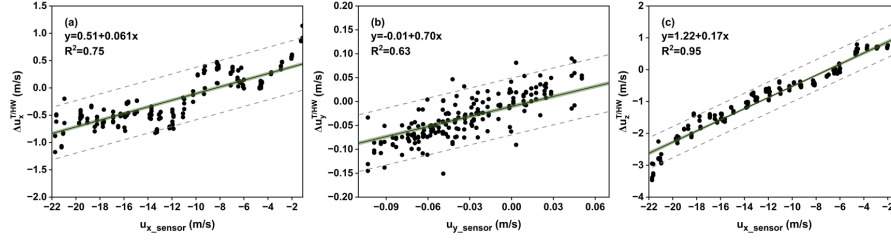
284 3.3 Rotor Interference on Anemometer Measurements

285 This study employs a regression fitting to explore the relationship between the false wind signals
286 generated by the UAV rotors airflow and the UAV's airspeed. Under tailwind and headwind conditions,
287 the false wind signals ($\Delta u_x^{T/HW}$, $\Delta u_y^{T/HW}$, and $\Delta u_z^{T/HW}$) on the anemometer resulting from the UAV
288 rotor -induced flows at both flight altitudes were aggregated and fitted as dependent variables in a
289 regression using u_{x_sensor} as the independent variable. As shown in Fig. 6 (a), (b) and (c), good linear
290 relationships were found between $\Delta u_x^{T/HW}$, $\Delta u_y^{T/HW}$, and $\Delta u_z^{T/HW}$ and the simulated velocity
291 components in the x -direction (u_{x_sensor}), respectively. The specific relationship is described by Eqs.
292 (12) to (14). Thus, using the UAV velocity components in x direction, the false wind signals caused by
293 the UAV propellers can be determined and removed from the raw measured wind velocity from the
294 anemometer.

295 For crosswind conditions, regressions were fitted with false wind signals (Δu_x^{CW} and Δu_z^{CW}) as
296 dependent variables and u_{x_sensor} as the independent variable in the same way (See Fig. 7). A linear
297 relationship was observed between the false wind signals in both x and z directions (Δu_x^{CW} and Δu_z^{CW})
298 and u_{x_sensor} , with the specific expressions in Eq. (15) and (16), respectively. As described in Sect. 3.2,
299 Δu_y^{CW} was sensitive to flight altitude under crosswind conditions, hence Δu_y^{CW} at 30 m and 1000 m
300 altitude ($\Delta u_{y(30)}^{CW}$ and $\Delta u_{y(1000)}^{CW}$) were regressed against u_{y_sensor} for the two flight altitudes
301 separately. The $\Delta u_{y(30)}^{CW}$ exhibited a linear relationship with u_{y_sensor} , as shown in Eq. (17). However,
302 the correlation coefficient between $\Delta u_{y(1000)}^{CW}$ and u_{y_sensor} was found to be lower than 0.5, indicating
303 that $\Delta u_{y(1000)}^{CW}$ may be considered independent of u_{y_sensor} . Therefore, the average value of $\Delta u_{y(1000)}^{CW}$
304 (0.006 m s^{-1}) was regarded as the $\Delta u_{y(1000)}^{CW}$ at this flight altitude.

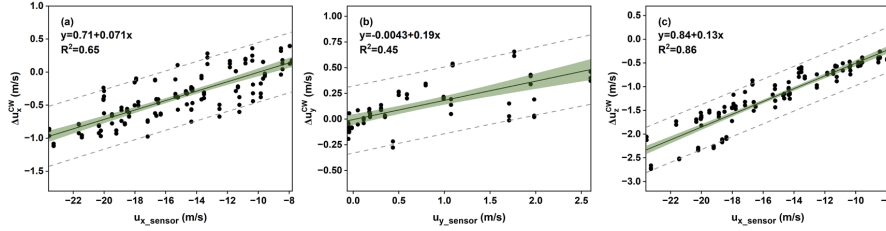
305 Despite the dependence of Δu_y^{CW} on flight altitudes, $\Delta u_{y(30)}^{CW}$ and $\Delta u_{y(1000)}^{CW}$ are confined to a
306 similar numeric range. Therefore, they may be roughly considered as representing Δu_y for lower
307 altitude (e.g., 0 to 500 m) and higher altitude (e.g., 500 to 1000 m), respectively.

308 Hence, for crosswind situations, the wind velocities in the x , y and z directions measured by the
309 anemometer are corrected by subtracting Δu_x^{CW} , Δu_z^{CW} and $\Delta u_{y(0-500)}^{CW}$ which are estimated from
310 $u_{x_sensor}/u_{y_sensor}$, or at relatively high flight altitudes using a constant value of 0.006 m s^{-1} for
311 $\Delta u_{y(501-1000)}^{CW}$.



312

313 **Figure 6:** Regression fit of artificial velocity ($\Delta u_x^{T/HW}$, $\Delta u_y^{T/HW}$ and $\Delta u_z^{T/HW}$) with $u_{x,sensor}$ for tailwind and
 314 headwind flight conditions at two altitudes. In the figure, simulation data are marked with black dots, fitted
 315 curves are indicated in black lines, the 95% confidence bands are identified as green shadows, and the 95%
 316 prediction bands are represented with gray dashed area.



317

318 **Figure 7:** Regression fit of false wind velocity signals Δu_x^{CW} , Δu_z^{CW} and $\Delta u_{y(0-500)}^{CW}$ with $u_{x,sensor}/u_{y,sensor}$
 319 for crosswind flight conditions at two altitudes. The symbols in the figure are the same as in Figure 6.

320
$$\Delta u_x^{T/HW} = 0.51 + 0.061 \times u_x, \quad (12)$$

321
$$\Delta u_y^{T/HW} = -0.01 + 0.70 \times u_y, \quad (13)$$

322
$$\Delta u_z^{T/HW} = 1.22 + 0.17 \times u_x, \quad (14)$$

323
$$\Delta u_x^{CW} = 0.71 + 0.071 \times u_x, \quad (15)$$

324
$$\Delta u_z^{CW} = 0.84 + 0.13 \times u_x, \quad (16)$$

325
$$\Delta u_{y(0-500)}^{CW} = -0.0043 + 0.19 \times u_y, \quad (h = 0 \sim 500 \text{ m}), \quad (17)$$

326
$$\Delta u_{y(501-1000)}^{CW} = 0.006, \quad (h = 501 \sim 1000 \text{ m}), \quad (18)$$

327 In Eq.(17) and (18), the variable h represents the flight altitude of the UAV.

328 3.4 The Overall Correction Algorithm

329 3.4.1 Motion and Attitude Compensation Correction of UAV

330 In addition to the false wind signals caused by propeller rotations, additional false wind velocity
 331 signals from the anemometer can be attributed to UAV movement and attitude (pitch, roll and yaw)
 332 changes during flight, and as such also need correction. When the UAV moves horizontally and vertically
 333 relative to the ground, the velocity vector measured by the anemometer is a vector combination of the



334 true wind velocity and the UAV's ground velocity. Consequently, the ground velocity of the UAV (v_x and
 335 v_z , with v_y always 0 due to no motion in the y direction) contributes false wind velocity components to
 336 measurements by the anemometer. Moreover, the UAV's flight attitude undergoes adjustments in the
 337 pitch, roll, and yaw Euler angles (θ , φ , and ψ , respectively), in order to compensate for aerodynamic
 338 resistance or adapt to flight plans. These adjustments lead to the anemometer measuring additional
 339 velocities resulting from the rotational rates of the attitude angles ($\mu(\theta)$ and $\mu(\varphi)$), with $\mu(\psi)$
 340 remaining zero due to the alignment of the rotational axis of ψ with the line connecting the UAV's center
 341 of gravity and the anemometer. Furthermore, the effect is further amplified by the distance (r) between
 342 the anemometer and the UAV's center of gravity. It is noteworthy that there is currently no reported
 343 correction algorithm for influence of attitude angle variations on anemometer wind velocity
 344 measurements from UAVs. To obtain accurate wind information, after eliminating the aforementioned
 345 interferences, the wind velocities (u_x , u_y and u_z) observed by the anemometer in the airframe coordinate
 346 (x , y and z directions) were transformed to the North-East-Down (NED) ground coordinate using the
 347 direction cosine matrix (DCM) as given in Eq. (19).

$$348 \begin{bmatrix} u_N \\ u_E \\ u_D \end{bmatrix} = \text{DCM}(\theta, \varphi, \psi) \left(\begin{bmatrix} u_x \\ u_y \\ u_z \end{bmatrix} + \begin{bmatrix} v_x \\ 0 \\ -v_z \end{bmatrix} + \begin{bmatrix} \mu(\theta) \\ -\mu(\varphi) \\ 0 \end{bmatrix} \right), \quad (19)$$

$$349 \text{DCM}(\theta, \varphi, \psi) = \begin{bmatrix} \cos(\psi) & -\sin(\psi) & 0 \\ \sin(\psi) & \cos(\psi) & 0 \\ 0 & 0 & 1 \end{bmatrix} \begin{bmatrix} \cos(\theta) & 0 & \sin(\theta) \\ 0 & 1 & 0 \\ -\sin(\theta) & 0 & \cos(\theta) \end{bmatrix} \begin{bmatrix} 1 & 0 & 0 \\ 0 & \cos(\varphi) & -\sin(\varphi) \\ 0 & \sin(\varphi) & \cos(\varphi) \end{bmatrix}, \quad (20)$$

350 where DCM is defined by Eq. (20); u_N , u_E and u_D refer to corrected North, East and Down
 351 components of wind velocity in the ground coordinate; v_x and v_z are the motion velocities of the UAV
 352 in the x and z directions respectively, which are directly provided by the GPS receiver output of the
 353 UAV or can be directly computed from the UAV longitude/latitude coordinate output; $\mu(\theta)$ and $\mu(\varphi)$
 354 represent the product of the pitch rate $\omega(\theta)$ and roll rate $\omega(\varphi)$, respectively, with the rotation radius r ,
 355 which is the distance between the anemometer and the center of gravity of the UAV, as defined in Eqs.
 356 (21) and (22). Due to the alignment of the anemometer's z -axis with that of the UAV, the variation in
 357 yaw ψ does not introduce false wind speed to signals from the anemometer in the airframe coordinate,
 358 resulting in $\mu(\psi)$ being equal to zero.

$$359 \mu(\theta) = \omega(\theta) \times r = \frac{d(\theta)}{dt} \times r, \quad (21)$$



$$360 \quad \mu(\varphi) = \omega(\varphi) \times r = \frac{d(\varphi)}{dt} \times r, \quad (22)$$

361 where $\omega(\theta)$ and $\omega(\varphi)$ are defined as the differentiation of θ and φ with respect to time t ,
 362 respectively.

363 3.4.2 Compensation Correction for Induced-Flow Disturbance by UAV Rotors

364 Based on the statistical analyses of the fluid simulation results in Sect. 3.3, the regression
 365 relationships between the false wind velocity signals generated by the propeller rotation and the
 366 simulated wind components sensed by the anemometer are integrated into the motion and attitude
 367 correction algorithm of UAV given in Eq. (19). The updated wind velocity correction algorithm is given
 368 as Eq. (23), whose second and third vectors on the right side of Eq. (23) represent the contributions of
 369 the propeller-induced wind signals under tailwind/headwind and crosswind conditions to u_x , u_y and u_z ,
 370 respectively, with A and B defined in Eqs. (17) and (18) to quantify their magnitudes. Since the measured
 371 wind velocities u_x and u_y from the anemometer correspond to the simulated u_{x_sensor} and u_{y_sensor} ,
 372 respectively, the regression relationships are modified by replacing u_x and u_y with u_{x_sensor} and u_{y_sensor} ,
 373 respectively. This yields the estimations of the false wind velocity signals, Δu_x , Δu_y and Δu_z , under
 374 different wind directions, in relation to u_x and u_y , as specified by Eqs. (12) - (18). Using Eq. 16, the actual
 375 wind velocity components, including north wind (u_N), east wind (u_E), and vertical wind (u_D), are
 376 computed after correcting for the effects of UAV's rotor propeller disturbance, motion, and attitude on
 377 the wind signal measurements from the anemometer.

$$378 \quad \begin{bmatrix} u_N \\ u_E \\ u_D \end{bmatrix} = \text{DCM}(\theta, \varphi, \psi) \left(\begin{bmatrix} u_x \\ u_y \\ u_z \end{bmatrix} - \begin{bmatrix} A \times \Delta u_x^{T/HW} \\ A \times \Delta u_y^{T/HW} \\ A \times \Delta u_z^{T/HW} \end{bmatrix} - \begin{bmatrix} B \times \Delta u_x^{CW} \\ B \times \Delta u_y^{CW} \\ B \times \Delta u_z^{CW} \end{bmatrix} + \begin{bmatrix} v_x \\ 0 \\ v_z \end{bmatrix} + \begin{bmatrix} -\mu(\theta) \\ \mu(\varphi) \\ 0 \end{bmatrix} \right), \quad (23)$$

$$380 \quad A = \left| \frac{u_x}{\sqrt{u_x^2 + u_y^2}} \right|, \quad (24)$$

$$381 \quad B = \left| \frac{u_y}{\sqrt{u_x^2 + u_y^2}} \right|, \quad (25)$$

382 3.5 Validation of the Correction Algorithm

383 A comparative experiment was designed to verify the effectiveness of the correction algorithm



384 described in Eq. (23). The experiment primarily compares three different wind data: the first is the three-
385 dimensional wind vector corrected only for UAV motion and attitude compensation (Eq. (19) and
386 denoted as \mathbf{V}_O), the second includes additional corrections for UAV rotor interference, along with motion
387 and attitude compensation (Eq. (23) and denoted as \mathbf{V}_R), and the third is the three-dimensional wind
388 directly measured by the meteorological tower (denoted as \mathbf{V}_T). The comparison experiment was
389 conducted with the UAV flying wind-boxes around the 80-meter meteorological tower within the
390 Experimental Base of the Beijing Key Laboratory of Cloud, Precipitation and Atmospheric Water
391 Resources. The meteorological tower was equipped with three-dimensional ultrasonic anemometers
392 positioned at heights of 30, 50, and 70 m, with one anemometer in the north and one in the south (see
393 Fig. 8). The UAV flew around the tower in a box flight path at a horizontal distance of about 10 m away
394 from the tower, at all three heights. Given the potential interference from near-surface vegetation on the
395 30-meter anemometer on the tower, wind velocities acquired by the UAV at 50 and 70 m heights during
396 steady flight intervals were analyzed herein.

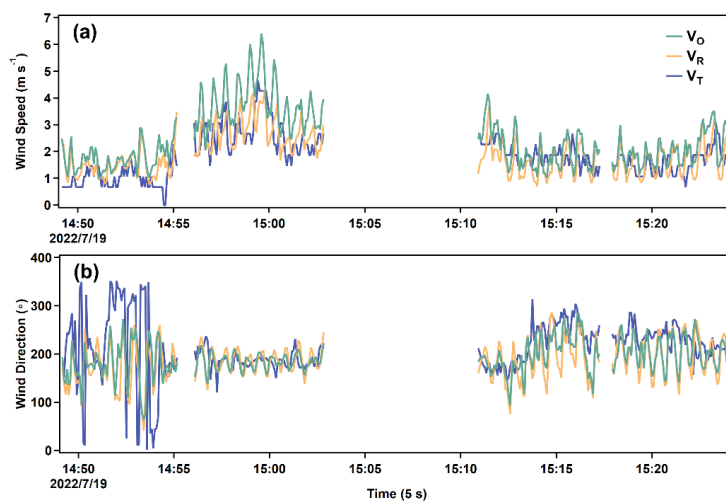


397
398 **Figure 8: Comparative experiment on wind measurements between the UAV and the meteorological tower.**

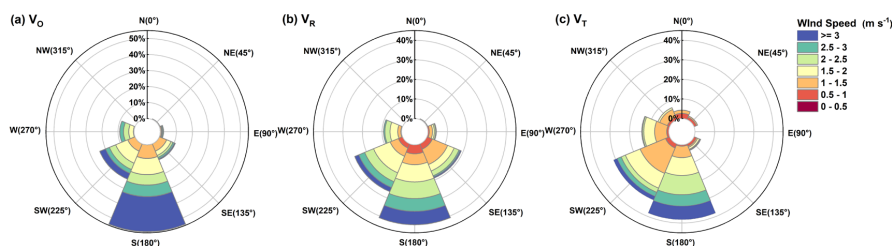
399 The results in Fig. 9 (a) demonstrate that at elevated wind speeds ($> 3 \text{ m s}^{-1}$), the wind velocities of
400 \mathbf{V}_R were substantially lower than that of \mathbf{V}_O . The root mean square relative errors between \mathbf{V}_R and \mathbf{V}_T ,
401 and \mathbf{V}_O and \mathbf{V}_T , are 0.28 and 0.37, respectively, with the former being approximately 24% smaller than
402 the latter. This indicates that the correction effect of Eq. (23) is especially pronounced in strong wind
403 conditions. In contrast, under gentle wind speeds ($\leq 3 \text{ m s}^{-1}$), \mathbf{V}_R exhibited greater consistency with \mathbf{V}_O



404 but there was still a significant down-revision in the average speed in V_R . The average wind speeds of
405 V_O , V_R , and V_T were 2.4, 1.91, and 1.81 m s^{-1} , respectively, with V_R exhibiting a 22% decrease compared
406 to V_O . The statistical analysis using the Wilcoxon signed-rank test confirmed a significant difference (p
407 < 0.01) in wind speed between V_O and V_T , whereas no significant differences ($p > 0.01$) were found
408 between V_R and V_T . This suggests that after compensating for UAV motion, attitude, and rotor
409 interference, the wind speed measured by the UAV anemometer is more closely aligned with that
410 measured directly by the meteorological tower. Moreover, under stronger winds, the wind direction
411 values of V_R , V_O , and V_T were relatively similar, yet at weaker winds, V_R showed a small low-bias (Fig.
412 9 (b)). Fig. 10 presents the wind rose diagrams, offering a detailed overview of the wind speed and
413 direction characteristics for V_R , V_O , and V_T . Compared to V_O , V_R showed a much improved match
414 between the corrected wind velocity and frequency distributions versus V_T (Fig. 10), both showing
415 predominant northerly winds. In summary, these analyses indicated that Eq. 16 can effectively correct
416 wind measurement biases induced by UAV disturbances, motion, and attitude changes, particularly at
417 higher wind speeds.



418
419 **Figure 9: Comparison of wind speed and wind direction time series for V_R , V_O , and V_T . (a) Comparison of**
420 **wind speed time series for V_R , V_O , and V_T . (b) Comparison of wind direction time series for V_R , V_O , and V_T .**
421 **(Note: The meteorological tower measured wind data at 5 s intervals, while the UAV-based measured and**
422 **corrected wind data was averaged using a 10 s sliding window before calculating 5 s mean values.)**



423

424 **Figure 10: Comparison of wind roses for V_R , V_O , and V_T .**

425 **4 Conclusions**

426 The scenarios involving direct measurements of wind fields within the atmospheric boundary layer
427 using multirotor UAVs have become progressively commonplace, heightening the significance of
428 accurate wind assessment. However, the rotor propellers during UAV flight introduce additional induced
429 flows at the anemometer location, leading to false wind speed signals. For the present UAV-anemometer-
430 payload configuration, a CFD-based method was used to simulate the process of the UAV wind
431 measurement platform during stable flights under headwind, tailwind, and crosswind conditions. The
432 analyses of induced airflows surrounding the anemometer led to a predictive tool for disturbance
433 airflows. Building upon the UAV motion and attitude correction algorithm, a correction algorithm was
434 proposed for the combined false wind signals from UAV rotor propeller disturbance, motion, and attitude
435 changes during UAV flights. Through comparison of the corrected wind speeds derived from
436 measurements taken from the UAV platform and concurrent three-dimensional wind measurements from
437 a nearby meteorological tower, the validity of the correction algorithm has been demonstrated. This
438 result presents a viable approach for directly measuring wind speeds with good accuracy from multirotor
439 UAV flights. Indeed, during the first application of the UAV measurement platform to determine
440 greenhouse gas emission rates from a large coking plant in one of the largest steelmaker in the country,
441 we have demonstrated that the emission rates determined on the basis of greenhouse gas concentration
442 and three-dimensional wind measurements match closely with emission rates determined from material
443 balance (Han T, 2023), again providing a secondary validation of such a correction algorithm.

444 In conclusion, this study represents a significant advancement in three-dimensional wind speed
445 measurement using UAV platforms, presenting a practical and effective method for direct and accurate
446 wind measurement. This technological breakthrough not only creates a strong foundation for precise



447 wind field measurements with UAVs but also provides potential avenues for the accurate quantification
448 of gaseous pollutant emissions based on UAV. The outcomes of this work carry considerable scientific
449 importance and offer valuable practical applications.

450

451 **Data availability:** Data will be made available on request.

452 **Acknowledgment:** This project was supported by a grant from the National Natural Science Foundation
453 of China Creative Research Group Fund (22221004).

454 **Declaration of competing interest:** The contact author has declared that none of the authors has any
455 competing interests.

456 **Reference**

457 Anderson, K. and Gaston, K. J.: Lightweight unmanned aerial vehicles will revolutionize spatial ecology,
458 *Front. Ecol. Environ.*, 11, 138-146, <https://doi.org/10.1890/120150>, 2013.

459 Barbieri, L., Kral, S. T., Bailey, S. C. C., Frazier, A. E., Jacob, J. D., Reuder, J., Brus, D., Chilson, P. B.,
460 Crick, C., Detweiler, C., Doddi, A., Elston, J., Foroutan, H., Gonzalez-Rocha, J., Greene, B. R., Guzman,
461 M. I., Houston, A. L., Islam, A., Kempainen, O., Lawrence, D., Pillar-Little, E. A., Ross, S. D., Sama,
462 M. P., Schmale, D. G., Schuyler, T. J., Shankar, A., Smith, S. W., Waugh, S., Dixon, C., Borenstein, S.,
463 and de Boer, G.: Intercomparison of small unmanned aircraft system (sUAS) measurements for
464 atmospheric science during the LAPSE-RATE campaign, *Sensors (Basel)*, 19,
465 <https://doi.org/10.3390/s19092179>, 2019.

466 Bonin, T. A., Chilson, P. B., Zielke, B. S., Klein, P. M., and Leeman, J. R.: Comparison and application
467 of wind retrieval algorithms for small unmanned aerial systems, *Geosci. Instrum., Methods Data Syst.*,
468 2, 177-187, <https://doi.org/10.5194/gi-2-177-2013>, 2013.

469 Booij, N., Ris, R. C., and Holthuijsen, L. H.: A third-generation wave model for coastal regions: 1. Model
470 description and validation, *J. Geophys. Res.: Oceans*, 104, 7649-7666,
471 <https://doi.org/10.1029/98JC02622>, 1999.

472 de Divitiis, N.: Wind estimation on a lightweight vertical-takeoff- and-landing uninhabited vehicle, *J.*
473 *Aircr.*, 40, 759-767, <https://doi.org/10.2514/2.3155>, 2003.



474 Drob, D. P., Emmert, J. T., Meriwether, J. W., Makela, J. J., Doornbos, E., Conde, M., Hernandez, G.,
475 Noto, J., Zawdie, K. A., McDonald, S. E., Huba, J. D., and Klenzing, J. H.: An update to the Horizontal
476 Wind Model (HWM): The quiet time thermosphere, *Earth Space Sci.*, 2, 301-319,
477 <https://doi.org/10.1002/2014EA000089>, 2015.

478 Elston, J., Argrow, B., Stachura, M., Weibel, D., Lawrence, D., and Pope, D.: Overview of small fixed-
479 wing unmanned aircraft for meteorological sampling, *J. Atmos. Ocean. Technol.*, 32, 97-115,
480 <https://doi.org/10.1175/Jtech-D-13-00236.1>, 2015.

481 Gonzalez-Rocha, J., Woolsey, C. A., Sultan, C., and De Wekker, S. F. J.: Sensing wind from quadrotor
482 motion, *J. Guid. Control Dyn.*, 42, 836-852, <https://doi.org/10.2514/1.G003542>, 2019.

483 Gousseau, P., Blocken, B., Stathopoulos, T., and van Heijst, G. J. F.: CFD simulation of near-field
484 pollutant dispersion on a high-resolution grid: A case study by LES and RANS for a building group in
485 downtown Montreal, *Atmos. Environ.*, 45, 428-438, <https://doi.org/10.1016/j.atmosenv.2010.09.065>,
486 2011.

487 Gryning, S. E., Holtslag, A. A. M., Irwin, J. S., and Sivertsen, B.: Applied dispersion modelling based
488 on meteorological scaling parameters, *Atmos. Environ.*, 21, 79-89, [https://doi.org/10.1016/0004-
489 6981\(87\)90273-3](https://doi.org/10.1016/0004-6981(87)90273-3), 1987.

490 Han T, X. C., Liu Y, Yang Y, Zhang Y, Huang Y, Gao X, Zhang X., Bao F, and Li S-M.: Application of a
491 new UAV measurement methodology to the quantification of CO₂ and CH₄ emissions from a major
492 coking plant, *Atmos. Meas. Tech.*, In Prep, 2023.

493 Hedworth, H., Page, J., Sohl, J., and Saad, T.: Investigating Errors Observed during UAV-Based Vertical
494 Measurements Using Computational Fluid Dynamics, *Drones*, 6, 253,
495 <https://doi.org/10.3390/drones6090253>, 2022.

496 Kim, M.-S. and Kwon, B. H.: Estimation of sensible heat flux and atmospheric boundary layer height
497 using an unmanned aerial vehicle, *Atmosphere*, 10, 363, <https://doi.org/10.3390/atmos10070363>, 2019.

498 Langelaan, J. W., Alley, N., and Neidhoefer, J.: Wind field estimation for small unmanned aerial vehicles,
499 *J. Guid. Control Dyn.*, 34, 1016-1030, <https://doi.org/10.2514/1.52532>, 2011.

500 Martin, S., Bange, J., and Beyrich, F.: Meteorological profiling of the lower troposphere using the
501 research UAV "M²AV Carolo", *Atmos. Meas. Tech.*, 4, 705-716, <https://doi.org/10.5194/amt-4-705-2011>,
502 2011.



- 503 McGonigle, A., Aiuppa, A., Giudice, G., Tamburello, G., Hodson, A., and Gurrieri, S.: Unmanned aerial
504 vehicle measurements of volcanic carbon dioxide fluxes, *Geophys. Res. Lett.*, 35,
505 <https://doi.org/10.1029/2007GL032508>, 2008.
- 506 Neumann, P. P. and Bartholmai, M.: Real-time wind estimation on a micro unmanned aerial vehicle
507 using its inertial measurement unit, *Sens. Actuators, A*, 235, 300-310,
508 <https://doi.org/10.1016/j.sna.2015.09.036>, 2015.
- 509 Niedzielski, T., Skjøth, C., Werner, M., Spallek, W., Witek, M., Sawiński, T., Drzeniecka-Osiadacz, A.,
510 Korzystka-Muskała, M., Muskała, P., and Modzel, P.: Are estimates of wind characteristics based on
511 measurements with Pitot tubes and GNSS receivers mounted on consumer-grade unmanned aerial
512 vehicles applicable in meteorological studies?, *Environ. Monit. Assess.*, 189, 1-18,
513 <https://doi.org/10.1007/s10661-017-6141-x>, 2017.
- 514 Nolan, P. J., Pinto, J., Gonzalez-Rocha, J., Jensen, A., Vezzi, C. N., Bailey, S. C. C., de Boer, G., Diehl,
515 C., Laurence, R., Powers, C. W., Foroutan, H., Ross, S. D., and Schmale, D. G.: Coordinated unmanned
516 aircraft system (UAS) and ground-based weather measurements to predict Lagrangian coherent
517 structures (LCSs), *Sensors (Basel)*, 18, <https://doi.org/10.3390/s18124448>, 2018.
- 518 Oktay, T. and Eraslan, Y.: Computational fluid dynamics (Cfd) investigation of a quadrotor UAV
519 propeller, *International Conference on Energy, Environment and Storage of Energy*, 21-25,
- 520 Palomaki, R. T., Rose, N. T., van den Bossche, M., Sherman, T. J., and De Wekker, S. F.: Wind estimation
521 in the lower atmosphere using multirotor aircraft, *J. Atmos. Ocean. Technol.*, 34, 1183-1191,
522 <https://doi.org/10.1175/JTECH-D-16-0177.1>, 2017.
- 523 Quan, Q.: *Introduction to Multicopter Design and Control*, Springer Singapore, 384 pp.,
524 <https://doi.org/10.1007/978-981-10-3382-7>, 2017.
- 525 Rautenberg, A., Graf, M. S., Wildmann, N., Platis, A., and Bange, J.: Reviewing wind measurement
526 approaches for fixed-wing unmanned aircraft, *Atmosphere*, 9, <https://doi.org/10.3390/atmos9110422>,
527 2018.
- 528 Riddell, K. D. A.: *Design, testing and demonstration of a small unmanned aircraft system (SUAS) and*
529 *payload for measuring wind speed and particulate matter in the atmospheric boundary layer*, University
530 of Lethbridge, Canada, 2014.
- 531 Rogers, K. and Finn, A.: Three-dimensional UAV-based atmospheric tomography, *J. Atmos. Ocean.*



- 532 Technol., 30, 336-344, <https://doi.org/10.1175/JTECH-D-12-00036.1>, 2013.
- 533 Seibert, P., Beyrich, F., Gryning, S. E., Joffre, S., Rasmussen, A., and Tercier, P.: Review and
534 intercomparison of operational methods for the determination of the mixing height, Atmos. Environ., 34,
535 1001-1027, [https://doi.org/10.1016/S1352-2310\(99\)00349-0](https://doi.org/10.1016/S1352-2310(99)00349-0), 2000.
- 536 Shaw, J. T., Shah, A. D., Yong, H., and Allen, G.: Methods for quantifying methane emissions using
537 unmanned aerial vehicles: a review, Philos. T. Roy. Soc. A, 379, <https://doi.org/10.1098/rsta.2020.0450>,
538 2021.
- 539 Shimura, T., Inoue, M., Tsujimoto, H., Sasaki, K., and Iguchi, M.: Estimation of wind vector profile
540 using a hexarotor unmanned aerial vehicle and its application to meteorological observation up to 1000
541 m above surface, J. Atmos. Ocean. Technol., 35, 1621-1631, <https://doi.org/10.1175/JTECH-D-17-0186.1>, 2018.
- 543 Soddell, J. R., McGuffie, K., and Holland, G. J.: Intercomparison of atmospheric soundings from the
544 Aerosonde and radiosonde, J. Appl. Meteorol., 43, 1260-1269, [https://doi.org/10.1175/1520-0450\(2004\)043<1260:IOASFT>2.0.CO;2](https://doi.org/10.1175/1520-0450(2004)043<1260:IOASFT>2.0.CO;2), 2004.
- 546 Spiess, T., Bange, J., Buschmann, M., and Vorsmann, P.: First application of the meteorological Mini-
547 UAV 'M²AV', Meteorol. Z., 16, 159-170, <https://doi.org/10.1127/0941-2948/2007/0195>, 2007.
- 548 Stewart, M., Martin, S., and Barrera, N., Barrera, N. (Ed.): Unmanned aerial vehicles: fundamentals,
549 components, mechanics, and regulations, Unmanned Aerial Vehicles, Nova Science Publishers,
550 Hauppauge, New York, USA, 71 pp.2021.
- 551 Stockie, J. M.: The mathematics of atmospheric dispersion modeling, SIAM Rev., 53, 349-372,
552 <https://doi.org/10.1137/10080991X>, 2011.
- 553 Thielicke, W., Hubert, W., Muller, U., Eggert, M., and Wilhelm, P.: Towards accurate and practical
554 drone-based wind measurements with an ultrasonic anemometer, Atmos. Meas. Tech., 14, 1303-1318,
555 <https://doi.org/10.5194/amt-14-1303-2021>, 2021.
- 556 van Hooff, T. and Blocken, B.: Coupled urban wind flow and indoor natural ventilation modelling on a
557 high-resolution grid: A case study for the Amsterdam ArenA stadium, Environ. Model. Softw., 25, 51-
558 65, <https://doi.org/10.1016/j.envsoft.2009.07.008>, 2010.
- 559 Vardoulakis, S., Fisher, B. E. A., Pericleous, K., and Gonzalez-Flesca, N.: Modelling air quality in street
560 canyons: a review, Atmos. Environ., 37, 155-182, [https://doi.org/10.1016/S1352-2310\(02\)00857-9](https://doi.org/10.1016/S1352-2310(02)00857-9),



561 2003.
562 Villa, T. F., Gonzalez, F., Miljievic, B., Ristovski, Z. D., and Morawska, L.: An overview of small
563 unmanned aerial vehicles for air quality measurements: Present applications and future perspectives,
564 Sensors (Basel), 16, <https://doi.org/10.3390/s16071072>, 2016.
565 Yang, Y., Zhou, J., Xie, C., Tian, W., Xue, M., Han, T., Chen, K., Zhang, Y., Liu, Y., and Huang, Y.: A
566 New Methodology for High Spatiotemporal Resolution Measurements of Air Volatile Organic
567 Compounds: From Sampling to Data Deconvolution, Environ. Sci. Technol., 58, 12488-12497, 2024.
568